

## Ultrafast Photoinduced Phase Change in SnSe

Benjamin J. Dringoli,<sup>1</sup> Mark Sutton<sup>1</sup>, Zhongzhen Luo,<sup>2,3</sup> Mercuri G. Kanatzidis,<sup>2</sup> and David G. Cooke<sup>1,\*</sup><sup>1</sup>Department of Physics, McGill University, Montreal, Quebec H3A2T8, Canada<sup>2</sup>Department of Chemistry, Northwestern University, Evanston, Illinois 60208, USA<sup>3</sup>Key Laboratory of Eco-Materials Advanced Technology, College of Materials Science and Engineering, Fuzhou University, Fuzhou 350108, People's Republic of China (Received 26 December 2022; revised 21 November 2023; accepted 31 January 2024; published 1 April 2024)

Time-resolved multiterahertz (THz) spectroscopy is used to observe an ultrafast, nonthermal electronic phase change in SnSe driven by interband photoexcitation with 1.55 eV pump photons. The transient THz photoconductivity spectrum is found to be Lorentzian-like, indicating charge localization and phase segregation. The rise of photoconductivity is bimodal in nature, with both a fast and slow component due to excitation into multiple bands and subsequent intervalley scattering. The THz conductivity magnitude, dynamics, and spectra show a drastic change in character at a critical excitation fluence of approximately 6 mJ/cm<sup>2</sup> due to a photoinduced phase segregation and a macroscopic collapse of the band gap.

DOI: 10.1103/PhysRevLett.132.146901

Tin selenide (SnSe) is a quasi-two dimensional semiconductor exhibiting record-setting thermoelectric properties, with a figure of merit  $ZT = 2.62$  along the in-plane  $b$  axis [1–5]. A polar analogue of black phosphorous, at room temperature SnSe has a layered, orthorhombic  $Pnma$  phase with zigzag and armchair ordering shown in Figs. 1(a) and 1(b), respectively. In the  $Pnma$  phase, it possesses an indirect band gap of 0.9 eV [6] and a direct gap of 1.21 eV [7], shown in Fig. 1(c). At  $T_c = 807$  K, a  $Pnma \rightarrow Cmcm$  structural phase transition occurs, reducing thermal conductivity due to phonon-phonon scattering arising from strong anharmonicity. The origin of this transition has been intensely studied in the past several years, being attributed to either a displacive transition typically seen in ferroelectrics or a dynamic order-disorder transition [8–16]. The displacive transition is primarily driven by atomic motion along the  $c$  axis [17], accompanied by phonon softening and an eventual collapse of terahertz (THz) frequency zone center optical phonons [17–19]. Very recent neutron scattering measurements, however, support a disordered high temperature phase with local contributions from the  $Pnma$  phase on length scales of a few unit cells [16]. Phonon anharmonicities in SnSe are driven by electronic bonding instabilities involving Se  $4p$  orbitals and Sn  $5s$  orbitals containing lone pair electrons [13,19–24], whose states comprise the photoaccessible  $\Gamma$ -valley valence band. Optical excitation can selectively perturb these deeper lying bands and reveal novel, thermally inaccessible phases.

Ultrafast scattering and spectroscopy can disentangle the complexity underlying these dynamic lattice instabilities [25–28], leading to a better understanding of the microscopic interactions underlying thermoelectric properties. Recently, structural probes such as ultrafast electron diffraction (UED) [29,30], time-resolved x-ray diffraction

(TRXRD) [31,32], and transient reflectivity measurements [33] have revealed novel, nonthermal structural dynamics following femtosecond excitation at photon energies of 1.55 eV ( $\lambda_p = 800$  nm). These have indicated subpicosecond transitions toward the  $Cmcm$  phase driven by displacive excitation of  $A_g$  phonons [33], domain formation mediated by photoinduced interlayer strain fields [29], bimodal polaron formation [30], and transient atomic

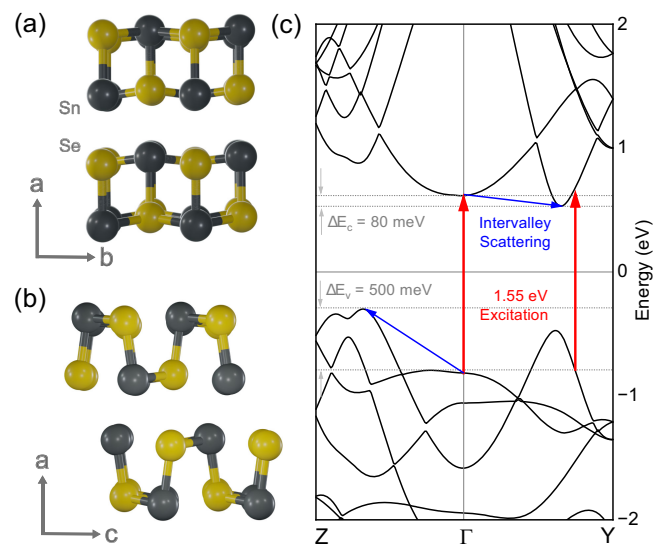


FIG. 1. (a),(b) SnSe layered atomic structure along the in-plane zigzag  $b$  axis and armchair  $c$  axis in the room temperature  $Pnma$  phase. (c)  $Pnma$ -phase SnSe electronic band structure from *ab initio* calculations using data provided from Ref. [5] with permission from the authors. Red arrows show carrier excitation from the 1.55 eV pump, blue arrows show postexcitation relaxation pathways to band extrema.

motions toward a thermally inaccessible *Immm* phase [31,32]. Given the diversity of structural phenomena indicated by these prior works, a complementary survey of the electronic behavior under these excitation conditions is needed.

In this Letter, we use ultrabroadband time-resolved THz spectroscopy to probe the electronic response of SnSe under identical excitation conditions as these previous ultrafast structural probe measurements ( $\lambda_p = 800$  nm,  $F = 0.1\text{--}13.2$  mJ/cm<sup>2</sup>). We observe non-Drude THz conductivity spectra exhibiting bimodal formation dynamics consistent with previous UED work reporting polaron formation after ultrafast excitation [30]. Moreover, we find evidence for an electronic phase transition occurring at a critical pump excitation fluence  $F_c \approx 6$  mJ/cm<sup>2</sup>, where THz conductivity magnitude, dynamics, and spectra change sharply. This excitation density is consistent with the proposed *Pnma*  $\rightarrow$  *Immm* destabilization threshold [31].

Time-resolved THz spectroscopy (TRTS) was performed using single-cycle, multiterahertz pulses shown in Supplemental Material, Fig. 1(a) [34]. These pulses were generated by a two-color laser plasma in dry air, formed by cofocusing 35 fs-duration fundamental (800 nm) and second harmonic (400 nm) pulses from a 1 kHz amplified Ti:sapphire femtosecond laser system [35–39]. These multiterahertz pulses contain Fourier components continuously covering a 1–20 THz spectral range (4–85 meV), as shown in Supplemental Material, Fig. 1(b) [34]. A schematic of the spectrometer is shown in Supplemental Material, Fig. 2 [34] and further details on the setup are provided in Ref. [25]. The SnSe sample was a 3 mm  $\times$  5 mm  $\times$  3.6 mm, high quality single crystal of SnSe grown using methods as described in Ref. [1], and from the same parent crystal as in Ref. [30]. The crystal was measured via reflection at normal incidence with the THz and pump pulses linearly polarized along the *b* axis. Other crystal orientations were measured, with results shown in Supplemental Material, Fig. 3 [34], however, no significant change in response was observed.

The reflected THz field was directly sampled in time  $t$  using air-biased coherent detection at various pump-probe delay times  $\tau$  [35,40]. Both the reflected field in the presence of a pump pulse,  $E_p(t, \tau)$ , and the differential  $\Delta E(t, \tau) = E_p(t, \tau) - E_r(t)$  are measured simultaneously in a double-modulation scheme [41], where  $E_r(t)$  is the reference THz field reflected from the unexcited sample. The pulse delays are implemented such that all points in the measured THz fields have experienced a constant  $\tau$ , so a Fourier transformation along the real time axis  $t$  is devoid of any convolution artifacts and directly provides a temporal snapshot of the frequency-dependent response [42]. Intrinsic artifacts that can appear in TRTS, as mentioned in Ref. [43], are not present (see Supplemental Material, Fig. 4 [34]) as carrier momentum relaxation times are

extremely short [44]. The pump-induced differential reflectivity  $\Delta\tilde{r}(\omega, \tau)/\tilde{r}_0(\omega) = \Delta E(\omega, \tau)/E_r(\omega) - 1$ , where  $\tilde{r}_0(\omega)$  is the static reflectivity, was subsequently extracted by Fourier analysis. The static  $\tilde{r}_0(\omega)$  is dominated by a single reststrahlen band for THz polarization parallel to the *b* axis [45], shown in Supplemental Material, Fig. 1 [34], which prohibits the extraction of the optical conductivity below  $\sim 5$  THz. The THz reflectivity is finally related to the pump-induced differential optical conductivity  $\Delta\tilde{\sigma}(\omega, \tau) = \Delta\sigma_1(\omega, \tau) + i\Delta\sigma_2(\omega, \tau)$  by modeling the photoexcited layer as a slab by [46]

$$\Delta\tilde{\sigma}(\omega, \tau) = \frac{1}{Z_0 d} \frac{(\Delta\tilde{r}/\tilde{r}_0)(\tilde{n}^2 - 1)}{(\Delta\tilde{r}/\tilde{r}_0)(1 - \tilde{n}) + 2}, \quad (1)$$

where  $d = 60$  nm is the pump penetration depth at  $\lambda = 800$  nm [47],  $Z_0 = 377 \Omega$  is the impedance of free space, and  $\tilde{n}(\omega)$  is the static complex THz refractive index [45]. Despite reports of saturable absorption in SnSe nanosheets at much lower peak powers [48], the pump absorption was found to be independent of excitation fluence and average heating of the sample surface was estimated by infrared imaging to be  $< 15^\circ\text{C}$ , shown in Supplemental Material, Figs. 5 and 6, respectively [34].

Two-dimensional  $\Delta\sigma_1(\omega, \tau)$  maps for frequencies above all phonon branches ( $\omega/2\pi > 5.5$  THz), where the electronic intraband response dominates, are shown in Fig. 2 for pump fluences of (a) 1.8 mJ/cm<sup>2</sup> and (b) 12.0 mJ/cm<sup>2</sup>. Additional 2D maps for varying fluences are presented in Supplemental Material, Fig. 7 [34]. In both low and high fluence regimes, the conductivity has Lorentzian character despite all assumptions of SnSe being a band semiconductor where the expectation is a simple Drude response. Such a broadened Lorentzian response can arise from phase heterogeneity and the formation of domains that favor conduction over smaller length scales (higher frequencies), which has been observed in SnSe at these fluences [29]. The optical conductivity of a heterogeneous phase system is usually described by effective medium theories (e.g., Bruggeman), and typically displays a monotonically increasing  $\sigma_1(\omega)$  from zero frequency [49]. However, here  $\sigma_1(\omega)$  exhibits a clear onset at the LO phonon energy of  $\sim 20$  meV ( $\sim 5$  THz). This could indicate that photoexcited carriers are polarons [50], as suggested by calculations showing strong electron-phonon coupling near  $\Gamma$  [51] and previous UED measurements indicating the formation of a 3D polaron with radius  $\sim 4.2$  Å after photoexcitation [30].

To quantify the evolution of spectral shape, we fit the data to a Lorentzian response given by

$$\Delta\tilde{\sigma}(\omega) = \frac{Ne^2}{m^*} \frac{\omega}{i(\omega_0^2 - \omega^2) + \omega\gamma}, \quad (2)$$

with  $Ne^2/m^*$  as the oscillator strength,  $\omega_0$  the resonance frequency, and  $\gamma$  the scattering rate. This simple

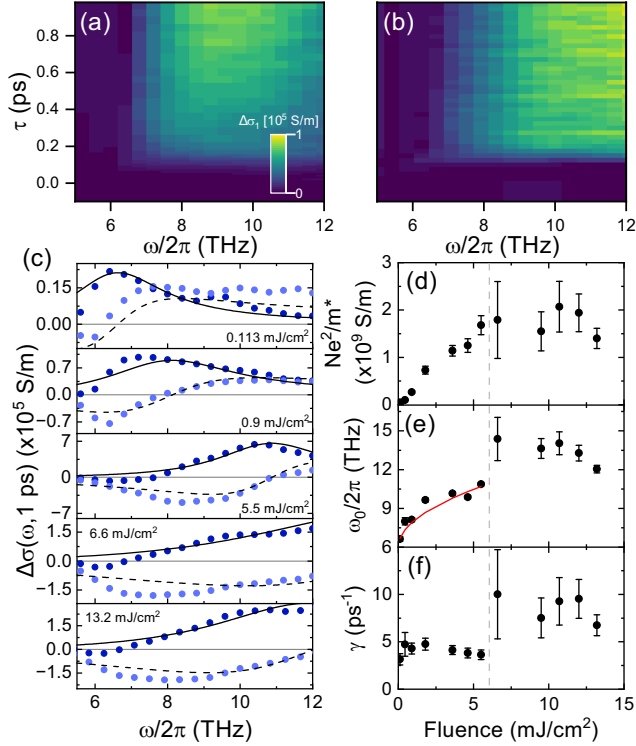


FIG. 2. (a),(b) Two-dimensional real conductivity  $\Delta\sigma_1(\omega, \tau)$  maps for 1.8 and 12.0  $\text{mJ}/\text{cm}^2$ . (c) Complex THz differential photoconductivity spectra  $\Delta\tilde{\sigma}(\omega, \tau) = \Delta\sigma_1(\omega, \tau) + i\Delta\sigma_2(\omega, \tau)$  for various fluences.  $\Delta\sigma_1(\omega, \tau = 1 \text{ ps})$  shown in dark colors,  $\Delta\sigma_2(\omega, \tau = 1 \text{ ps})$  shown in light colors, and Lorentzian fits shown in black solid and dashed lines. Note the significant difference in vertical axis scales. Fluence dependence of the (d) Lorentzian oscillator strength  $Ne^2/m^*$ , (e) center frequency  $\omega_0$ , and (f) linewidth  $\gamma$ .  $\omega_0$  is fitted with a scaled  $\sqrt{F}$  function, shown in red and discussed in the text.

phenomenological model fits both  $\sigma_1$  and  $\sigma_2$  reasonably well over the entire fluence regime for all times, as shown in Fig. 2(c) and in Supplemental Material, Fig. 8 [34]. The fit parameters  $Ne^2/m^*$ ,  $\omega_0$ , and  $\gamma$  for all fluences are shown in Figs. 2(d)–2(f), respectively. Two fluence regimes are identified: a low ( $F < 6.6 \text{ mJ}/\text{cm}^2$ ) and a high ( $F \geq 6.6 \text{ mJ}/\text{cm}^2$ ) fluence regime. In the low fluence regime,  $Ne^2/m^*$  increases linearly and monotonically with fluence, as expected for unsaturated interband excitation of charge carriers. The scattering rate  $\gamma$  remains relatively constant in this fluence range, reflecting consistency of the absorption pathways shown in Fig. 1(c) for these fluences. The fitted  $\omega_0$  scales with an approximately  $\sqrt{F}$  dependence just above the LO phonon energy. Localization of charges is implied in a Lorentzian response, however, the increase of  $\omega_0$  with fluence is inconsistent with models of weak localization [52] or backscattering [53]. Instead, this implies a plasmonic origin where such a  $\omega_0 \propto \sqrt{F}$  dependence is expected for a heterogeneous medium, provided there is isolation of neighboring conducting domains such

that depolarization fields contribute [49,54]. The long time relaxation of the system, shown in Supplemental Material, Fig. 9 [34], occurs on a  $\sim 150 \text{ ps}$  timescale, consistent with previous measurements reporting interband recombination [55]. This relaxation is also seen in the redshifting of the spectral peak at long times shown in Supplemental Material, Fig. 10 [34], again consistent with a system of heterogeneous conductive media. At a critical fluence  $F_c = 6.6 \text{ mJ}/\text{cm}^2$ , a discontinuous increase in  $\omega_0$  and  $\gamma$  occurs while  $Ne^2/m^*$  saturates. This sudden change suggests a charge density-driven electronic phase transition occurring on ultrafast timescales.

Further evidence for an electronic phase transition is seen in the dynamics of  $\sigma_1(\omega, \tau)$ , monitored at  $\omega/2\pi = 10 \text{ THz}$ , far above all phonon branches and where  $\Delta\sigma$  is dominated by electronic excitations. Figures 3(a)–3(e) show the clear bimodal dynamics in the subpicosecond manifestation of photoconductivity. In the low fluence regime, there are two distinct components: a 40 fs instrument response-limited rise after photoexcitation and a slower  $\sim 200 \text{ fs}$  rise. Examining the *Pnma* band structure shown in Fig. 1(c), we can classify pump absorption into two main channels: (1) excitation into the high effective mass, nondispersive bands about the  $\Gamma$  point which subsequently undergo interband scattering to the lower-mass band extrema; and (2) excitation of hot, mobile charge carriers distributed throughout the Brillouin zone that cool via intraband relaxation. The  $\Gamma$  valley carriers have an effective mass of

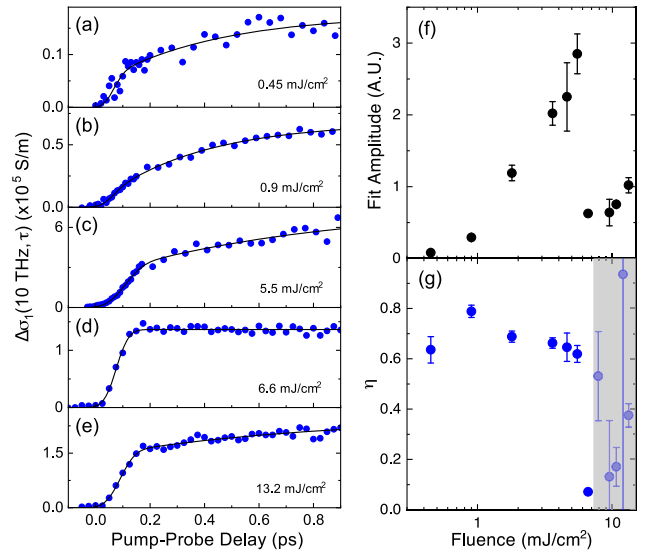


FIG. 3. (a)–(e)  $\Delta\sigma_1(\omega, \tau)$  dynamics at  $\omega/2\pi = 10 \text{ THz}$  for indicated pump fluences  $F$ . Rate equation model fits [Eq. (3)] are shown as black lines. Note the differences in vertical axis scaling. (f)  $\Delta\sigma_1(10 \text{ THz}, 1 \text{ ps})$  as a function of pump fluence, showing approximately linear scaling below  $F_c$  and a sharp drop with little scaling above  $F_c$ . (g) Fitted proportion of carriers deposited in band extrema  $\eta$  [Eq. (3)] as a function of fluence showing sharp drop near  $F_c$ .



$1.20m_e$  [2], eight times that of band extrema along  $\Gamma$ -Y and  $\Gamma$ -Z at  $0.15m_e$  [56]. Therefore, the measured THz conductivity is dominated by  $n_{\text{free}}$ , with the slow rise representing the scattering of heavier  $n_{\Gamma}$  carriers to the extrema, enabled through the high electron-phonon coupling near the  $\Gamma$  point [51]. The conductivity dynamics can therefore be well fit by a two-component rate equation model:

$$\begin{aligned} \frac{dn_{\Gamma}(t)}{dt} &= \eta \exp[-(t/\sqrt{2}\tau_p)^2] - n_{\Gamma}(t)\gamma_{\text{inter}}, \\ \frac{dn_{\text{free}}(t)}{dt} &= (1 - \eta) \exp[-(t/\sqrt{2}\tau_p)^2] + n_{\Gamma}(t)\gamma_{\text{inter}}, \\ \Delta\sigma_1(t) &= A \left( \frac{e\tau}{m_f^*} n_{\text{free}}(t) + \frac{e\tau}{m_{\Gamma}^*} n_{\Gamma}(t) \right). \end{aligned} \quad (3)$$

Here,  $n_{\Gamma}$ ,  $n_{\text{free}}$  are the populations in the  $\Gamma$  and mobile bands, respectively,  $\eta$  is the fraction of charge carriers excited into the  $\Gamma$  valley,  $\tau_p$  is the pump pulse duration,  $e$  is the electron charge,  $A$  is an amplitude scaling factor, and  $m^*$  are the effective masses. As a simplifying assumption, the momentum scattering time  $\tau$  is assumed to be 20 fs for both populations [44]. The intervalley scattering rate,  $\gamma_{\text{inter}} \approx 1\text{--}2$  THz, is typical of polar semiconductors at room temperature [57]. When  $F \geq 6.6$  mJ/cm<sup>2</sup>, the same fluence where the spectra sharply blueshifted, the magnitude of the response  $A$  drops sharply as shown in Fig. 3(f). At the same fluence, the slow scattering process and associated rise in conductivity, represented by  $\eta$  and shown in Fig. 3(g), vanishes and only recovers slightly at the higher fluences. This indicates the sudden elimination of intervalley scattering from the  $\Gamma$  valley. Such a drastic change in the magnitude, spectra, and dynamics of intraband conductivity at  $F_c$  is a strong indication of a photoinduced, ultrafast change of macroscopic phase over THz wavelength length scales.

A photoinduced *Pnma-Immm* structural phase transition was recently observed in SnSe accompanied by a fluence-dependent softening of  $A_g$  phonon modes [31]. This Peierls-like structural instability is driven by the removal of electrons in nondispersive electronic bands derived from both Se  $4p_x$  orbitals and Sn  $5s$  orbitals [32], which form the nondispersive bands at  $\Gamma$  [13]. The authors estimated the *Pnma* phase is fully destabilized in favor of the *Immm* phase at a photoexcited carrier density of 0.2 holes per formula unit, corresponding to  $9 \times 10^{20}$  cm<sup>-3</sup>. The corresponding critical density from these measurements is estimated as  $n_c = F_c(1 - R)\eta\lambda/hcd \approx 2 \times 10^{21}$  cm<sup>-3</sup>, in fair agreement. The transition to the *Immm* phase is expected to cause band structure renormalization and a closure of the electronic band gap, leading to semimetallic electronic dispersion [31]. A transition to a semimetallic band structure could explain the fixed finite-frequency spectral peak above  $F_c$  as a new interband THz absorption would appear in the mid-IR. Additional support for this idea is the relatively

fluence-independent conductivity above  $F_c$  shown in Fig. 2(d), which would be expected for a system whose gap is collapsed as excitation only serves to heat the charge distribution. While a recent time-resolved angle-resolved photoemission spectroscopy (TRARPES) study of SnSe observed some evidence of spectral weight within the gap as early as 40 fs following photoexcitation, the 800 nm excitation fluence was significantly below  $F_c$  at 0.95 mJ/cm [58]. Our observations and critical fluence are in excellent agreement with very recent calculations on SnSe accounting for quantum anharmonicities arising from the photoexcited electron-hole plasma [59].

In conclusion, time-resolved THz spectroscopy was used to probe the ultrafast electronic response of SnSe under femtosecond optical excitation. The transient THz optical conductivity was Lorentzian in character whose resonant frequency is carrier density dependent. This suggests photocarrier localization into heterogeneous conducting domains and phase coexistence on the nanoscale, driven by optical excitation and the removal of bonding electrons. Bimodal photoconductivity dynamics were observed and could be explained by multi-valley excitation into both free and localized states related to the nondispersive bands derived from the Sn  $5s$ -Se  $4p$  hybridization. At a critical fluence of  $F_c \approx 6$  mJ/cm<sup>2</sup>, the spectra, dynamics, and magnitude of the THz conductivity change drastically indicating a macroscopic change of phase. The vanishing of intervalley scattering and the near constant conductivity magnitude with a further increase of pump fluence suggests a collapse of the band gap, which is consistent with a recent study suggesting SnSe moves toward a thermally inaccessible *Immm* phase. This motivates further high fluence TRARPES measurements and time-resolved spatial probes of nanoscale conductivity to potentially resolve this novel, transient phase of SnSe.

B. J. D. and D. G. C. are grateful for the SnSe electronic band structure data from Ref. [5] provided by D. Rybkovskiy and for conversations with B. Siwick. This work was supported through funding by NSERC and Mitacs programs. The Northwestern University personnel and research work was supported by the Department of Energy, Office of Science, Basic Energy Sciences under Grant No. DE-SC0024256 (design and synthesis of thermoelectric materials).

\*Corresponding author: david.cooke2@mcgill.ca

- [1] L. D. Zhao, S. H. Lo, Y. S. Zhang, H. Sun, G. J. Tan, C. Uher, C. Wolverton, V. P. Dravid, and M. G. Kanatzidis, *Nature (London)* **508**, 373 (2014).
- [2] R. Q. Guo, X. J. Wang, Y. D. Kuang, and B. L. Huang, *Phys. Rev. B* **92**, 115202 (2015).
- [3] C. Chang, G. J. Tan, J. Q. He, M. G. Kanatzidis, and L. D. Zhao, *Chem. Mater.* **30**, 7355 (2018).

- [4] M. M. Alsalama, H. Hamoudi, A. Abdala, Z. K. Ghouri, and K. M. Youssef, *Rev. Adv. Mater. Sci.* **59**, 371 (2020).
- [5] V. Tayari, B. V. Senkovskiy, D. Rybkovskiy, N. Ehlen, A. Fedorov, C.-Y. Chen, J. Avila, M. Asensio, A. Perucchi, P. Di Pietro, L. Yashina, I. Fakh, N. Hemsworth, M. Petrescu, G. Gervais, A. Grüneis, and T. Szkopek, *Phys. Rev. B* **97**, 045424 (2018).
- [6] K. Patel, G. Solanki, K. Patel, V. Pathak, and P. Chauhan, *Eur. Phys. J. B* **92**, 1 (2019).
- [7] T. Q. Dang, *Phys. Status Solidi A* **86**, 421 (1984).
- [8] J. M. Skelton, L. A. Burton, S. C. Parker, A. Walsh, C. E. Kim, A. Soon, J. Buckeridge, A. A. Sokol, C. R. A. Catlow, A. Togo, and I. Tanaka, *Phys. Rev. Lett.* **117**, 075502 (2016).
- [9] D. Bansal, J. W. Hong, C. W. Li, A. F. May, W. Porter, M. Y. Hu, D. L. Abernathy, and O. Delaire, *Phys. Rev. B* **94**, 054307 (2016).
- [10] G. D. Tang, J. Liu, J. Zhang, D. Li, K. H. Rara, R. Xu, W. Q. Lu, J. Z. Liu, Y. S. Zhang, and Z. Z. Peng, *ACS Appl. Mater. Interfaces* **10**, 30558 (2018).
- [11] C. Chang and L. D. Zhao, *Mater. Today Phys.* **4**, 50 (2018).
- [12] F. Liu, P. Parajuli, R. Rao, P. C. Wei, A. Karunarathne, S. Bhattacharya, R. Podila, J. He, B. Maruyama, G. Priyadarshan, J. R. Gladden, Y. Y. Chen, and A. M. Rao, *Phys. Rev. B* **98**, 224309 (2018).
- [13] J. Hong and O. Delaire, *Mater. Today Phys.* **10**, 100093 (2019).
- [14] P. Wu, F. R. Fan, M. Hagihala, M. Kofu, K. L. Peng, Y. Ishikawa, S. Lee, T. Honda, M. Yonemura, K. Ikeda, T. Otomo, G. Y. Wang, K. Nakajima, Z. Sun, and T. Kamiyama, *New J. Phys.* **22**, 083083 (2020).
- [15] Y. Lu, F. W. Zheng, Y. Yang, P. Zhang, and D. B. Zhang, *Phys. Rev. B* **103**, 014304 (2021).
- [16] B. Jiang, J. Neu, D. Olds, S. A. Kimber, K. Page, and T. Siegrist, *Nat. Commun.* **14**, 3211 (2023).
- [17] T. Chattopadhyay, J. Pannetier, and H. G. Vonscherner, *J. Phys. Chem. Solids* **47**, 879 (1986).
- [18] U. Aseginolaza, R. Bianco, L. Monacelli, L. Paulatto, M. Calandra, F. Mauri, A. Bergara, and I. Errea, *Phys. Rev. Lett.* **122**, 075901 (2019).
- [19] T. Lanigan-Atkins, S. Yang, J. L. Niedziela, D. Bansal, A. F. May, A. A. Puretzky, J. Y. Y. Lin, D. M. Pajerowski, T. Hong, S. Chi, G. Ehlers, and O. Delaire, *Nat. Commun.* **11**, 1 (2020).
- [20] L. D. Zhao, C. Chang, G. J. Tan, and M. G. Kanatzidis, *Energy Environ. Sci.* **9**, 3044 (2016).
- [21] Y. Xiao, C. Chang, Y. L. Pei, D. Wu, K. L. Peng, X. Y. Zhou, S. K. Gong, J. Q. He, Y. S. Zhang, Z. Zeng, and L. D. Zhao, *Phys. Rev. B* **94**, 125203 (2016).
- [22] J. S. Kang, H. Wu, M. Li, and Y. J. Hu, *Nano Lett.* **19**, 4941 (2019).
- [23] C. W. Li, J. Hong, A. F. May, D. Bansal, S. Chi, T. Hong, G. Ehlers, and O. Delaire, *Nat. Phys.* **11**, 1063 (2015).
- [24] J. L. Ma, Y. N. Chen, and W. Li, *Phys. Rev. B* **97**, 205207 (2018).
- [25] Y. Lan, B. J. Dringoli, D. A. Valverde-Chávez, C. S. Ponseca, M. Sutton, Y. He, M. G. Kanatzidis, and D. G. Cooke, *Sci. Adv.* **5**, eaaw5558 (2019).
- [26] M. R. Otto, L. P. René de Cotret, D. A. Valverde-Chavez, K. L. Tiwari, N. Émond, M. Chaker, D. G. Cooke, and B. J. Siwick, *Proc. Natl. Acad. Sci. U.S.A.* **116**, 450 (2019).
- [27] M. Liu, H. Y. Hwang, H. Tao, A. C. Strikwerda, K. Fan, G. R. Keiser, A. J. Sternbach, K. G. West, S. Kittiwatanakul, and J. Lu, *Nature (London)* **487**, 345 (2012).
- [28] D. Fausti, R. Tobey, N. Dean, S. Kaiser, A. Dienst, M. C. Hoffmann, S. Pyon, T. Takayama, H. Takagi, and A. Cavalleri, *Science* **331**, 189 (2011).
- [29] W. Wang, L. Wu, J. Li, N. Aryal, X. Jin, Y. Liu, M. Fedurin, M. Babzien, R. Kupfer, and M. Palmer, *npj Quantum Mater.* **6**, 1 (2021).
- [30] L. P. René de Cotret, M. R. Otto, J.-H. Pöhls, Z. Luo, M. G. Kanatzidis, and B. J. Siwick, *Proc. Natl. Acad. Sci. U.S.A.* **119**, e2113967119 (2022).
- [31] Y. Huang, S. Yang, S. Teitelbaum, G. De la Peña, T. Sato, M. Chollet, D. Zhu, J. L. Niedziela, D. Bansal, A. F. May, A. M. Lindenberg, O. Delaire, D. A. Reis, and M. Trigo, *Phys. Rev. X* **12**, 011029 (2022).
- [32] Y. Huang, S. Teitelbaum, S. Yang, G. De la Peña, T. Sato, M. Chollet, D. Zhu, J. L. Niedziela, D. Bansal, A. F. May, A. M. Lindenberg, O. Delaire, M. Trigo, and D. A. Reis, *Phys. Rev. Lett.* **131**, 156902 (2023).
- [33] Y. Han, J. Yu, H. Zhang, F. Xu, K. Peng, X. Zhou, L. Qiao, O. V. Misochko, K. G. Nakamura, and G. M. Vanacore, *J. Phys. Chem. Lett.* **13**, 442 (2022).
- [34] See Supplemental Material at <http://link.aps.org/supplemental/10.1103/PhysRevLett.132.146901> for additional descriptions of the experiment, sample, analysis, and results for all fluences tested.
- [35] J. Dai, X. Xie, and X.-C. Zhang, *Phys. Rev. Lett.* **97**, 103903 (2006).
- [36] D. Cook and R. Hochstrasser, *Opt. Lett.* **25**, 1210 (2000).
- [37] K.-Y. Kim, J. H. Glowina, A. J. Taylor, and G. Rodriguez, *IEEE J. Quantum Electron.* **48**, 797 (2012).
- [38] M. D. Thomson, V. Blank, and H. G. Roskos, *Opt. Express* **18**, 23173 (2010).
- [39] P. U. Jepsen, D. G. Cooke, and M. Koch, *Laser Photonics Rev.* **5**, 124 (2011).
- [40] I.-C. Ho, X. Guo, and X.-C. Zhang, *Opt. Express* **18**, 2872 (2010).
- [41] K. Iwaszczuk, D. G. Cooke, M. Fujiwara, H. Hashimoto, and P. U. Jepsen, *Opt. Express* **17**, 21969 (2009).
- [42] H. Němec, F. Kadlec, and P. Kužel, *J. Chem. Phys.* **117**, 8454 (2002).
- [43] J. Orenstein and J. S. Dodge, *Phys. Rev. B* **92**, 134507 (2015).
- [44] A. S. Chaves, R. L. Gonzalez-Romero, J. J. Melendez, and A. Antonelli, *Phys. Chem. Chem. Phys.* **23**, 900 (2021).
- [45] I. Efthimiopoulos, M. Berg, A. Bande, L. Puskar, E. Ritter, W. Xu, A. Marcelli, M. Ortolani, M. Harms, J. Muller, S. Speziale, M. Koch-Muller, Y. Liu, L. D. Zhao, and U. Schade, *Phys. Chem. Chem. Phys.* **21**, 8663 (2019).
- [46] F. A. Hegmann and K. P. Lui, in *Ultrafast Phenomena in Semiconductors VI* (SPIE, San Diego, 2002), Vol. 4643, pp. 31–41.
- [47] L. Makinistian and E. A. Albanesi, *Phys. Status Solidi B* **246**, 183 (2009).
- [48] G. M. Wang, W. F. Zhang, F. Xing, K. Z. Han, H. N. Zhang, and S. G. Fu, *Infrared Phys. Technol.* **108**, 103349 (2020).

- [49] P. Kužel and H. Němec, *J. Phys. D* **47**, 374005 (2014).
- [50] W. H. Sio and F. Giustino, *Nat. Phys.* **19**, 629 (2023).
- [51] F. Caruso, M. Troppenz, S. Rigamonti, and C. Draxl, *Phys. Rev. B* **99**, 081104(R) (2019).
- [52] K. Lee, A. J. Heeger, and Y. Cao, *Phys. Rev. B* **48**, 14884 (1993).
- [53] N. V. Smith, *Phys. Rev. B* **64**, 155106 (2001).
- [54] H. J. Joyce, J. L. Boland, C. L. Davies, S. A. Baig, and M. B. Johnston, *Semicond. Sci. Technol.* **31**, 103003 (2016).
- [55] T. W. Yan, Y. P. Han, Q. Fu, T. T. Xu, S. W. Yin, W. Z. Wu, and W. L. Liu, *Opt. Mater.* **108**, 110440 (2020).
- [56] A. Das, A. Kumar, and P. Banerji, *J. Phys. Condens. Matter* **32**, 265501 (2020).
- [57] J. Shah, B. Deveaud, T. C. Damen, W. T. Tsang, A. C. Gossard, and P. Lugli, *Phys. Rev. Lett.* **59**, 2222 (1987).
- [58] M. Okawa, Y. Akabane, M. Maeda, G. Tan, L.-D. Zhao, M. G. Kanatzidis, T. Suzuki, M. Watanabe, J. Xu, and Q. Ren, *Scr. Mater.* **223**, 115081 (2023).
- [59] S. Stefano, G. Marini, and M. Calandra, *J. Phys. Chem. Lett.* **14**, 9329 (2023).